Available online at www.sciencedirect.com
ScienceDirect
Journal of Magnetic Resonance 190 (2008) 124–134
JMR Journal of Magnetic Resonance
www.elsevier.com/locate/jmr

A loop resonator for slice-selective in vivo EPR imaging in rats

Hiroshi Hirata [a,*], Guanglong He [b], Yuanmu Deng [b], Ildar Salikhov [b], Sergey Petryakov [b], Jay L. Zweier [b]

[a] Department of Electrical Engineering, Yamagata University, Yonezawa, Yamagata 992-8510, Japan
[b] Center for Biomedical EPR Spectroscopy and Imaging, Davis Heart and Lung Research Institute, and the Division of Cardiovascular Medicine, Department of Internal Medicine, Ohio State University, Columbus, OH 43210, USA

Received 19 January 2007; revised 24 October 2007
Available online 30 October 2007

Abstract

A loop resonator was developed for 300 MHz continuous-wave electron paramagnetic resonance (CW-EPR) spectroscopy and imaging in live rats. A single-turn loop (55 mm in diameter) was used to provide sufficient space for the rat body. Efficiency for generating a radiofrequency magnetic field of 38 $\mu T/W^{1/2}$ was achieved at the center of the loop. For the resonator itself, an unloaded quality factor of 430 was obtained. When a 350 g rat was placed in the resonator at the level of the lower abdomen, the quality factor decreased to 18. The sensitive volume in the loop was visualized with a bottle filled with an aqueous solution of the nitroxide spin probe 3-carbamoyl-2,2,5,5-tetramethyl-3-pyrrolin-1-yloxy (3-CP). The resonator was shown to enable EPR imaging in live rats. Imaging was performed for 3-CP that had been infused intravenously into the rat and its distribution was visualized within the lower abdomen.

Keywords: Resonator; RF magnetic field; In vivo EPR imaging; Slice-selective image; Rat

1. Introduction

Electron paramagnetic resonance (EPR) imaging is a powerful modality for investigating free radicals in small animals [1–3]. While EPR imaging on mice is available, larger animals such as rats are needed for disease models in biomedical applications. For example, microsurgery is easier in a rat heart than in a mouse heart. Moreover, when the spatial resolution of EPR imaging is limited, larger subjects such as rats are more useful for investigating the internal distribution of free radicals in a specific organ. To accommodate rats in EPR imaging, a larger radiofrequency (RF) resonator is necessary, and lower RF frequencies would be needed, since electromagnetic waves would need to penetrate deeper to visualize free radicals. This is because electromagnetic loss and the penetration depth in biological tissues depend on the RF frequency [4]. Under these circumstances, it is considered that an RF frequency of 250 MHz or 300 MHz is suitable for EPR spectroscopy and imaging with larger subjects with a cross-section of 50–60 mm, such as with an adult rat. However, there have been only a few reports on RF resonators that are suitable for EPR spectroscopy and imaging and that can provide sufficient space to accommodate the body of a rat [5–8]. A variety of MRI coils with a frequency range of 300–400 MHz have been reported for small animal and human imaging [9–17]. Those reports are important sources for the development of EPR resonators in the same frequency band. In MRI at 7 T or 9 T, the body of the subject animal is generally oriented parallel to the static magnetic field. However, in EPR imaging, the body is often oriented perpendicular to the static magnetic field. There are several differences in the requirements for resonators used for CW-EPR. At 300 MHz, high continuous power levels of up to 6 W are needed for optimum sensitivity. Coupling must be efficient and precisely adjustable to achieve the

* Corresponding author. Fax: +81 238 26 3299.
E-mail address: hhirata@yz.yamagata-u.ac.jp (H. Hirata).

1090-7807/$ - see front matter © 2007 Elsevier Inc. All rights reserved.
doi:10.1016/j.jmr.2007.10.012

requisite detector biasing of the reflection bridge, and the design must not impair or distort the 100 kHz magnetic field modulation required for phase-sensitive detection. Furthermore, for enhanced sensitivity over a given region, it is highly desirable to select a region-sensitive resonator that will have an increased filling factor and sensitivity in the region of interest. The application of longitudinally-detected electron spin resonance (LODESR) to rats has also been reported [18,19]. Moreover, proton-electron double resonance (PEDRI), also known as Overhauser-enhanced MRI (OMRI), can be used for free radical imaging in rats [8,19–21]. Nevertheless, the scope of RF resonators reported for EPR imaging in rats has been quite limited and there is a need for resonators that are more suitable for sensitive and stable operation in this important in vivo model.

Most EPR imaging in small animals uses a continuous-wave (CW) approach. While slice-selective image acquisition is possible in a pulsed protocol in MRI, CW-EPR imaging requires three-dimensional (3D) data acquisition to construct a slice-selective image. However, 3D EPR imaging usually takes longer than the acquisition time of 2D EPR imaging with a standard scheme for obtaining the projection data in a CW method [22]. If the sensitive volume of an RF resonator is slice-selective, 2D EPR imaging with such an RF resonator could be useful for obtaining quasi-slice EPR images. Recently, pulsed EPR imagers at a low-magnetic field have been developed for small rodents [23–25]. However, pulsed EPR techniques in animal experiments are limited to spin probes that have longer relaxation times, e.g., currently on the order of microseconds. It is still difficult to measure free radicals with shorter relaxation times (broader absorption linewidth) using a pulsed protocol.

An RF resonator that can provide sufficient space for rats is needed in biomedical applications of EPR spectroscopy and imaging. In addition, to make slice-selective EPR imaging possible, we tested a loop resonator using a bottle phantom and rats. Our experimental findings show that this resonator enables in vivo slice-selective EPR imaging of free radicals in living rats.

2. Methods

2.1. Resonator design

For EPR imaging in rats, the following requirements had to be met: (i) electromagnetic waves should penetrate to a depth sufficient for a rat, (ii) the RF resonator must accommodate a rat, (iii) the RF resonator must have a high-power capability of at least 1 W, (iv) a slice-selective RF magnetic field is desirable, and (v) the configuration of the RF resonator should be suitable for the future implementation of automatic tuning and matching control. Since we need to have a larger loop to accommodate a rat, a weaker RF magnetic field is expected for this larger loop and also a lower quality factor of the resonator with a subject rat. Since these require a higher RF power to maximize the observed EPR signals, we set requirement (iii).

For requirement (i), we set the frequency to 300 MHz. This allowed us to achieve a penetration depth suitable for rats [4]. This frequency corresponds to that of proton MRI at 7 T. This means that there are no problems regarding the penetration depth of electromagnetic waves in biological tissues. For requirement (ii), the diameter of the resonator was determined to be 55 mm. This diameter provides sufficient space for rats with a body weight of 350 g. To satisfy the high-power capability in requirement (iii), a half-wave line balun was used to feed the resonator. This decreases the radiation of electromagnetic waves from the lines and makes the resonator less sensitive to environmental conditions, e.g., the motion of the subject animal and workers in the laboratory. To meet requirement (iv), a single-turn loop was used. Volume coils such as a loop-gap resonator (LGR) and a birdcage coil have a broad distribution of RF magnetic field in a subject. If a LGR has a very short axial length, it would be similar to a single-turn loop in terms of RF magnetic field. For requirement (v), a capacitive matching circuit was used, since varactor diodes can be implemented with the present matching circuit in the future.

An NMR probe with a balanced circuit scheme has been reported by Murphy-Boesch and Koretsky [26]. This NMR probe was tested for in vivo ^{31}P NMR spectroscopy with rat kidney at 97.3 MHz. The NMR probe can be considered to be a balanced circuit, when the following assumptions are satisfied. The first assumption is that the quality factor of the sample circuit (a parallel-resonant circuit consisting of a loop and a capacitor) is high enough to make the impedance of the matching capacitors small compared with the 50 Ω input impedance. The second assumption is that the coil-to-ground parasitics are identical between each side of the sample coil and ground. Since the sample coil is usually symmetrical, the second assumption is generally satisfied with a balanced circuit. In contrast, the first assumption is no longer valid when the carrier frequency goes up to 300 MHz. The quality factor of the parallel-resonant circuit that is filled with a rat's abdomen is very low. The NMR probe described in Ref. [26] becomes an unbalanced circuit with the conditions of CW-EPR spectroscopy and imaging of live rats at 300 MHz. Based on the general design of the NMR probe reported by Murphy-Boesch and Koretsky, we designed and tested an improved RF resonator that is rigorously balanced to the ground. A half-wave line balun and a scheme of parallel matching circuit were key to make the resonator balanced and less sensitive to the environment around the resonator. The details of the resonator are described below.

2.2. Loop resonator

Fig. 1A shows the configuration of the loop resonator and its feeding circuit. A single-turn coil (inner diameter of 55 mm and wire thickness of 1.6 mm) was connected

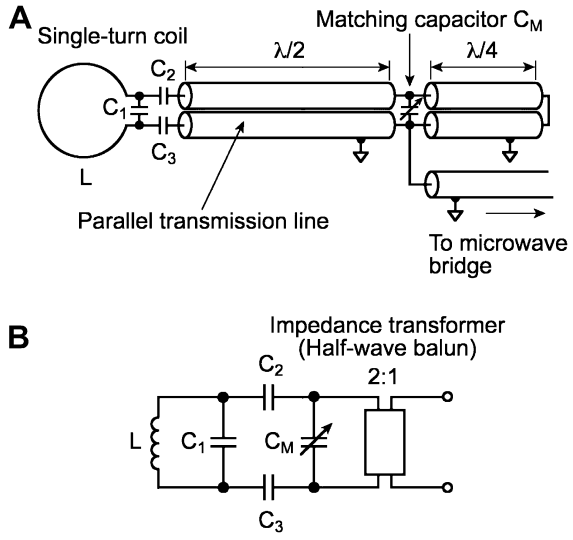

Fig. 1. (A) Configuration of a loop resonator. The wavelength λ in the coaxial lines depends on the frequency and the dielectric constant of the insulator in the cables. Semi-rigid coaxial cables (6.4 mm thick) were used for the resonator. The capacitors (C_1–C_3) were made of CuFlon® substrates. The single-turn loop was 55 mm in diameter and 1.6 mm thick. A half-wave balun is formed with serially connected $\lambda/4$ coaxial cables. (B) Equivalent electrical circuit. A transmission line of $\lambda/2$ is not shown because it does not transform the impedance of the load (L, C_1–C_3). Losses of the loop (energy deposition in biological tissue, radiation, and ohmic loss) are not shown in this equivalent circuit.

to a parallel-plate capacitor that was made from a copper-laminated polytetrafluoroethylene (PTFE) substrate, CuFlon®. This combination is similar to the multi-coil parallel-gap resonators used in EPR and NMR imaging [27]. Since the combination of a loop and a capacitor gives a parallel-resonant circuit with high impedance at its resonance frequency, it is difficult to critically couple the parallel-resonant circuit to a parallel transmission line (characteristic impedance of 100 Ω in our resonator) unless an impedance matching circuit is used. Therefore, a capacitive divider was used to simplify the coupling adjustment. However, this capacitive divider cannot be adjusted during experiments, since the parallel-plate capacitors were made from CuFlon® substrates. A non-magnetic trimmer capacitor (C_M in Fig. 1A, NMAJ55HV, Voltronics, Denville, NJ) was used to adjust the impedance matching of the resonator consisting of a single-turn loop and the capacitor C_1. The parallel transmission line and the balun were made from semi-rigid coaxial cables (6.4 mm in diameter and characteristic impedance of 50 Ω). Since the insulator in the coaxial lines was PTFE (dielectric constant of 2.1), the wavelength in the coaxial lines was 0.69 m at 300 MHz. The CuFlon® substrate (CF-A-20-7-7, Polyflon Company, Norwalk, CT) of the capacitor C_1 had an area of 36 mm^2 and was 0.51 mm thick (1.3 pF). For capacitors C_2 and C_3, the area and thickness of CuFlon® were 19 mm^2 and 0.51 mm (0.7 pF). We experimentally adjusted the areas of the substrates to achieve the intended resonance frequency and critical coupling. To obtain a critical coupling of the resonator with a subject rat, the trimmer capacitor C_M was manually adjusted.

Fig. 1B shows an electrical circuit equivalent to the loop resonator. A half-wave transmission line is not shown in Fig. 1B, since it does not transform the impedance at one end to the other end. Even if a trimmer capacitor C_M is adjustable, critical coupling of the resonator could only be achieved when the other capacitors were appropriately adjusted. For several EPR resonators, remote tuning and matching circuits with varactor diodes have been reported [28–31]. Since the varactor diodes are usually used in applications with small signals, e.g., tuning of RF oscillators and radio/television receivers, non-linearity of the varactor diodes will appear in high-power applications. This requires us to investigate the tuning and matching circuits with varactor diodes that have high-power capabilities. Before the loop resonator is fully implemented with varactor diodes, we thereby made and tested the resonator without functions of automatic tuning and matching control. In the present work, the concept of the loop resonator and its feeding circuit was investigated along with its feasibility for slice-selective in vivo EPR spectroscopy and imaging of living rats.

2.3. Calculations of currents and RF magnetic fields

To understand the characteristics of the loop resonator, we conducted numerical calculations on the current of the loop and RF magnetic fields generated near the loop. We used the method of moments to estimate the current of the loop excited at 300 MHz. Fig. 2A shows the numerical model of the single-turn loop, which was divided into 18 segments. Eighteen points were also defined at both ends of the segments. We defined the voltage source at point 0 in Fig. 2A. The parameters of the loop were described in the previous section. In the numerical simulation, we used WIRE89 which is a program for calculating the radiation and scattering of thin wire structures [32]. First, currents of the loop were estimated. RF magnetic fields of the loop were then calculated from the currents of the loop. RF magnetic field B_1 perpendicular to static magnetic field B_0 was calculated by Biot–Savart's law. Since the RF magnetic field parallel to the static magnetic field (Z-direction) does not contribute to EPR excitation, RF magnetic fields in the X- and Y-directions were taken into account. Finally, the distribution of RF magnetic energy density was estimated by the square of RF magnetic field, B_1, since the signal intensities of EPR spectra are proportional to the RF magnetic energy density in the loop.

2.4. Phantom

To visualize the sensitive volume in the loop, a cylindrical bottle filled with 1 mM 3-carbamoyl-2, 2, 5, 5-tetramethyl-3-pyrrolin-1-yloxy (3-CP) in half water/half phosphate-buffered saline (PBS) solution was measured. This solution was intended to mimic the loss of electromagnetic waves in biological tissues. The bottle was 49 mm in diameter and

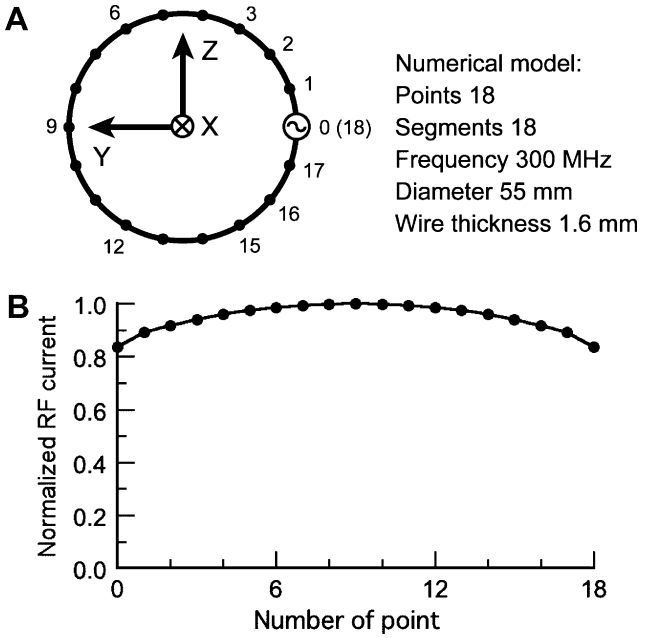

Fig. 2. (A) Modeling of a single-turn loop for the method of moments. The voltage source was placed at point 0. The conductivity of copper was used for the loop. To surround the loop, a vacuum medium was assumed in the numerical computations. (B) Estimated current in the wire of the loop. Values of current at each point were normalized by the maximum value at point 9.

140 mm long. It contained approximately 240 ml of 3-CP solution that was freshly prepared. Since the diameter of the bottle was slightly smaller than the inner diameter of the loop, the bottle was wrapped in a piece of paper to keep the bottle at the center of the loop.

2.5. Preparation of the rat

Male Sprague-Dawley rats with body weights of 300–350 g were used. To minimize side effects on the redox status, anesthesia was induced using 3% isoflurane in air [33]. The trachea was exposed by an incision under the neck, a cannula was inserted into the trachea from the mouth and the rat was artificially ventilated with a tidal volume of 1.5 ml at a rate of 90 cycles/min. The left jugular vein was then cannulated for delivery of the redox probe 3-CP. After the rat was positioned in the resonator and EPR system, a bolus volume of 3 ml of 100 mM 3-CP half water/half PBS solution was administered through the jugular vein within 2–3 min, and EPR imaging was then conducted. All surgical procedures were approved by the Institutional Animal Care and Use Committee at Ohio State University, Columbus, Ohio, and conformed to the Guide for the Care and Use of Laboratory Animals (NIH publication No. 86–23, revised 1985).

2.6. EPR hardware

A home-built 300-MHz CW-EPR imager at Ohio State University was used in the experiments. In this CW-EPR imager, a resistive magnet with a Helmholtz coil configuration was used with a modulation coil and orthogonal gradient coils. The gap of the Helmholtz coil pair for magnetic field modulation was 123 mm. The maximum field modulation was 0.3 mT, and the available maximum field gradients were more than 0.8 mT/cm. Homogeneity of the magnetic modulation field with an error of $<5\%$ was achieved within a spherical volume with a diameter of 44 mm. Also, an error of $<10\%$ was observed within a sphere 64 mm in diameter. Field gradients with an error of less than 10% covered 89 mm along the X-axis, 76 mm along the Y-axis, and 51 mm along the Z-axis. A reflection-type EPR bridge was used, and no reference arm was employed as shown in Fig. 3. While the reference arm in the bridge is helpful to improve the SNR of measured spectra at low power by maintaining optimized detector bias, little if any improvement is seen at high power operation, >100 mW. For this reason and to facilitate operation no reference arm was used. An RF synthesizer (Fluke 6080/AN, Fluke Corp., Everett, WA) was used as an RF source. An RF carrier signal was amplified by a power amplifier (amp1 in Fig. 3, LA0005-10, Delta RF Electronics, Reno, NV), and amplified RF waves were

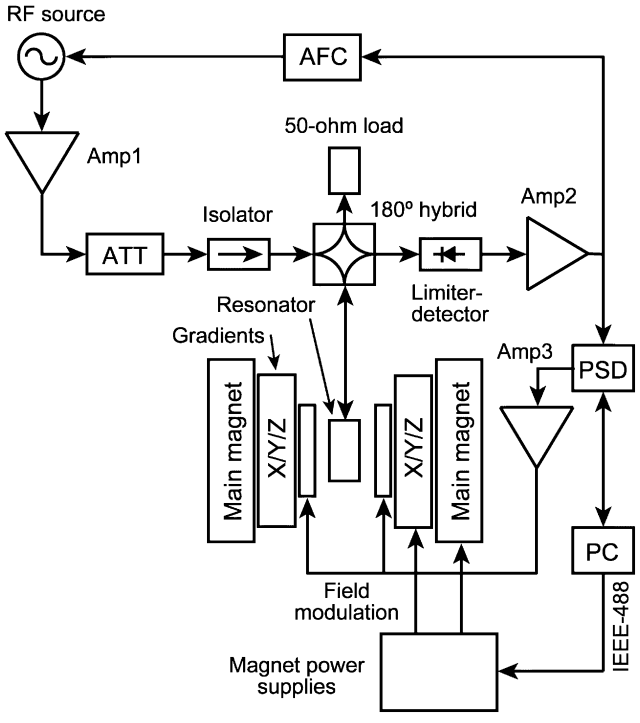

Fig. 3. Block diagram of a 300-MHz EPR imaging instrument. Details of the RF components in the bridge were describes in Section 2.6. The Output signals of the detector were amplified with a home-built low-noise amplifier (amp2), and phase-sensitive detection for EPR spectra was performed with a lock-in amplifier (PSD). Data transfer was controlled with a personal computer (PC) via IEEE-488 interface bus. The lock-in amplifier also outputs the modulation signal into the power amplifier (amp 3, P3000, Hafler division of Rockford Corporation, Temple, AZ) for the modulation coils. A PC controlled the power supplies (262NH and 261P, Copley Controls Corporation, Canton, MA) via IEEE-488 interface bus for the main magnet and the gradient coils.

then applied to the resonator through a 180-degree hybrid (H-1-4, M/A-COM, Lowell, MA). An isolator (a combination of a 50 Ω load and a circulator, CT-1559-OT, UTE Microwave, Ashbury Park, NJ) was inserted between the attenuator and the hybrid. Since the hybrid is less sensitive to a static magnetic filed generated by the magnet used in the imaging hardware, we used the 180-degree hybrid, instead of a circulator that is sensitive to a static magnetic field. Microwave power applied to the resonator is available up to 2.0 W, and it was adjusted with an attenuator (50HT42, Alan Industries, Columbus, IN). A limiter-Schottky detector (DSL101-848, Herotek, San Jose, CA) was used for RF detection. This detector contains a limiter and a Schottky diode in a single case. This does not differ from a combination of individual elements, i.e., a limiter and a detector. Automatic frequency control was available in our EPR bridge. A signal for field modulation at 100 kHz was delivered from a module of a Bruker EPR spectrometer (ER-023M, Bruker BioSpin, Billerica, MA), and phase-sensitive detection for first-derivative EPR absorption spectra was performed. Utilizing this instrument, good quality EPR spectra could be obtained on phantoms and living rats as described below.

2.7. EPR imaging

For EPR imaging of the bottle phantom, the field of view (FOV) was set to 70 mm. The static magnetic field B_0 was in the Z-direction. The bottle phantom and the body of the rat were oriented in the X-direction, and were perpendicular to the static magnetic field B_0. The single-turn loop of the resonator was in the ZY-plane. 2D EPR imaging was performed in the ZY- and ZX-planes. The measurement parameters in EPR imaging were as follows: scanning field 2.1 mT, magnetic field gradient 0.3 mT/cm, magnetic field modulation 0.1 mT, modulation frequency 100 kHz, scan time 10.5 s, time constant 81.9 ms, applied microwave power 2.0 W, number of projections 64, and acquisition time 11 min. The EPR absorption spectrum of 3-CP shows a triplet, and its lowest field absorption peak was used for image reconstruction.

To test the resonator, spin probes were intravenously infused into the rat. The single-turn loop of the resonator was placed at the level of the lower abdomen of the rat. After 3-CP probes were infused into the rat, we measured four sets of projections in the ZY-plane, and then a set of projections in the ZX-plane. Each set of projections was acquired within a 4 min interval. The measurement parameters in EPR imaging of the rat were as follows: scanning field 1.4 mT, magnetic field gradient 0.2 mT/cm, FOV 7 cm, magnetic field modulation 0.1 mT, scan time 10.5 s, time constant 40.9 ms, applied microwave power 1.6 W, number of projections 16, and acquisition time 4 min.

All of the projections were preprocessed and deconvolved before image reconstruction. In preprocessing, respiratory noise was compressed in the Fourier domain by removing the corresponding respiratory frequency. The deconvolved projections were then back-projected to obtain a reconstructed image using a filtered back-projection algorithm.

3. Results

3.1. Quality factor and efficiency for generating an RF magnetic field

With no sample in the loop, the resonator had the following characteristics: resonance frequency 301 MHz, quality factor 430, and efficiency for generating an RF magnetic field at the center of the loop 38 $\mu T/W^{1/2}$. The RF magnetic field in a loop was measured by using a perturbing metal sphere [34]. With the bottle phantom, the resonance frequency and quality factor of the resonator were, respectively, 290 MHz and 26. When an anesthetized rat was placed in the single-turn loop, the resonance frequency and quality factor fell to 281 MHz and 18, respectively.

3.2. Currents and RF magnetic fields

The distribution of current flowing in the loop at 300 MHz is shown in Fig. 2B. The maximum intensity of current was at the middle of the loop (point 9 in Fig. 2A) and the minimum intensity was at the location of the voltage source (point 0 in Fig. 2A). Since the circumference of the loop (173 mm) is not negligibly small in comparison to the wavelength of the electromagnetic waves (1 m in vacuum at 300 MHz), the distribution of RF current is no longer uniform over the loop. From the current distribution in Fig. 2B, RF magnetic fields around the loop were computed numerically. Fig. 4 shows the distributions of RF magnetic energy for the ZY-plane with an offset of the X-direction, i.e., 5, 10, 15, and 20 mm from the center of the loop. RF magnetic fields were computed in an area of 70 mm × 70 mm. In each distribution, the density of RF magnetic energy was normalized by the maximum value in Fig. 4A (offset of 5 mm in the X-direction). Since the maximum intensity of current is at the middle point of the loop, the intensity of the RF magnetic field and its energy density reached the highest point in the vicinity of the middle point of the loop. The distributions of RF magnetic energy were not asymmetric, as shown in Fig. 4, because the RF magnetic field parallel to the static magnetic field was excluded in this simulation. We assumed a vacuum medium around the loop in the numerical simulations. Thus, the distributions will be altered due to the presence of eddy currents and electromagnetic loss when a subject animal or a bottle phantom is placed in the loop. However, the results of the simulations presented here can be helpful for understanding the fundamental characteristics of RF magnetic fields generated by the loop resonator. If the simulation of RF magnetic fields in biological tissues is required, the finite element method (FEM) or the finite difference time domain (FDTD)

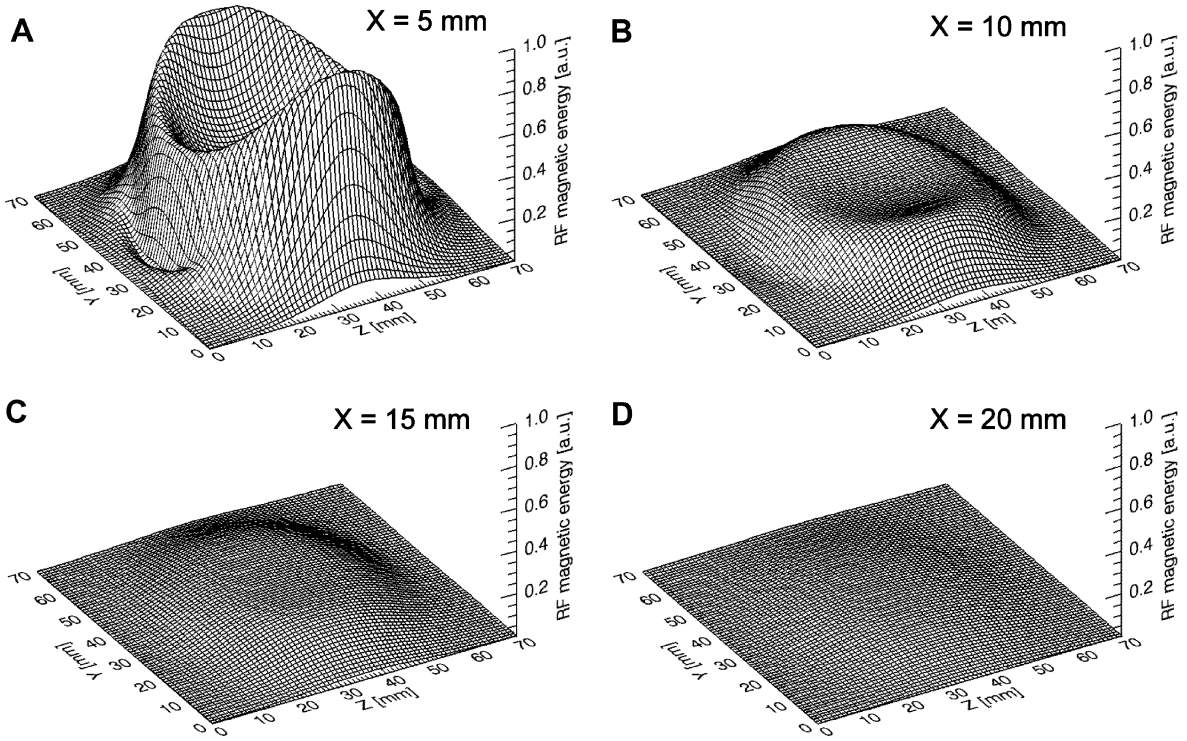

Fig. 4. Distribution of RF magnetic energy in the ZY-plane. The center of the loop was placed at the center of the calculated area, which was 70 mm × 70 mm. RF magnetic fields were calculated from the estimated distribution of current in Fig. 2B. RF magnetic field parallel to the static magnetic field (Z-direction) was excluded in this computation. (A) Distribution with an offset of 5 mm in the X-direction. (B) Distribution with an offset of 10 mm in the X-direction. (C) Distribution with an offset of 15 mm in the X-direction. (D) Distribution with an offset of 20 mm in the X-direction.

method with a modeling of biological subjects can be used to obtain precisely estimated RF magnetic fields [15].

3.3. Sensitivity distribution in the loop

To visualize the sensitive area in the loop, a bottle phantom was measured [35]. Fig. 5A shows a zero-gradient first-derivative EPR absorption spectrum for the bottle phantom. A signal-to-noise ratio (SNR) of 128 was achieved in a single scan under the following conditions: scan time 60.2 s, scanning field 5.0 mT, time constant 0.327 s, magnetic field modulation 0.1 mT, and microwave power 2.0 W. The peak-to-peak linewidth ΔB_{pp} of the first-derivative EPR absorption spectrum in Fig. 5A was 0.14 mT. Fig. 5B shows the lowest field absorption peak of 3-CP in the lower abdomen of the rat. After 3-CP probes were injected into the rat, this spectrum was measured with a scanning field of 2.1 mT. Other parameters were noted in EPR imaging for the rat. Periodic noise in the baseline was observed due to the respiratory motion of the rat. However, the SNR of the spectrum in Fig. 5B was sufficient for obtaining EPR images. Since AFC was operating in this measurement, a dominant cause of this periodic noise could be related to impedance mismatching of the resonator. This could be further suppressed with automatic matching control, also called automatic coupling control [28–31].

Fig. 6B shows an EPR image of the bottle phantom in the ZY-plane (Fig. 6A). A practically homogeneous distribution of sensitivity in the loop was obtained. The profile in the Y-direction shows an inhomogeneous distribution of sensitivity. Since the RF current in the loop was not uniform, the weaker current in the loop near the capacitor C_1 results in a relatively weak RF magnetic field. Fig. 6C shows an EPR image of the bottle phantom in the ZX-plane. The effective width of the profile (full width at half maximum) in the X-direction was approximately 17 mm. These images suggest that the sensitivity of the loop is slice-selective. In our previous report for the surface coil resonator at 1.05 GHz, the effective width of the sensitive region corresponding to Fig. 6C was similar to the radius of the loop or little longer [35]. In contrast, our results in Fig. 6C suggest that the loop resonator reported here is more slice-selective (the effective width was 31% of the diameter of the loop) than the surface coil resonator at 1.05 GHz.

3.4. EPR imaging in an anesthetized rat

As shown in Fig. 7A, an anesthetized rat was placed in the single-turn loop, and the loop was placed at the level of the lower abdomen of the rat. The sensitive region of the loop would include the lower liver, kidneys and bladder. Fig. 7B shows four EPR images in the ZY-plane for

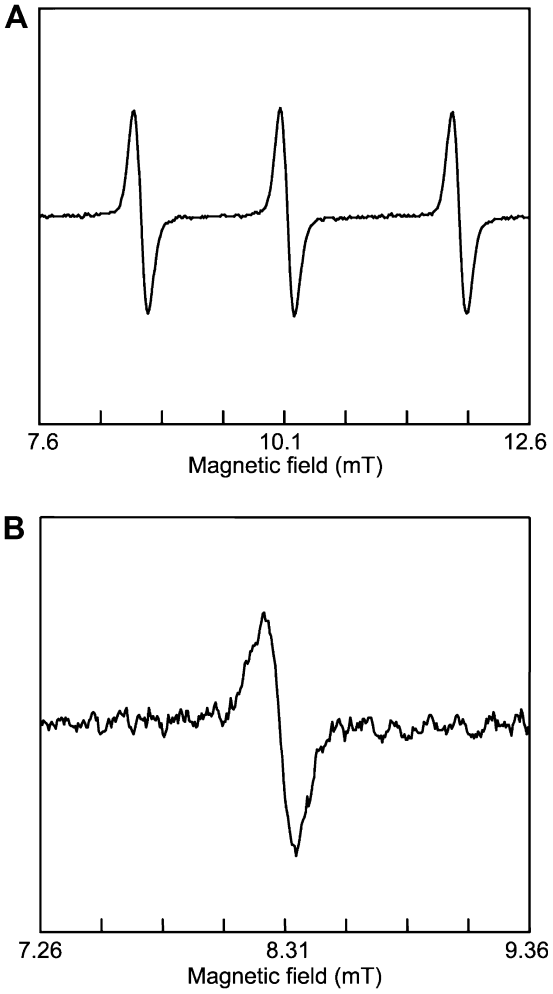

Fig. 5. (A) EPR spectrum of 3-carbamoyl-2,2,5,5-tetramethyl-3-pyrrolin-1-yloxy (3-CP). A cylindrical bottle 49 mm in diameter and 140 mm long was filled with 1 mM 3-CP in half water/half PBS solution and measured with the resonator at 300 MHz. (B) Lower absorption peak of 3-CP in the lower abdomen of the rat.

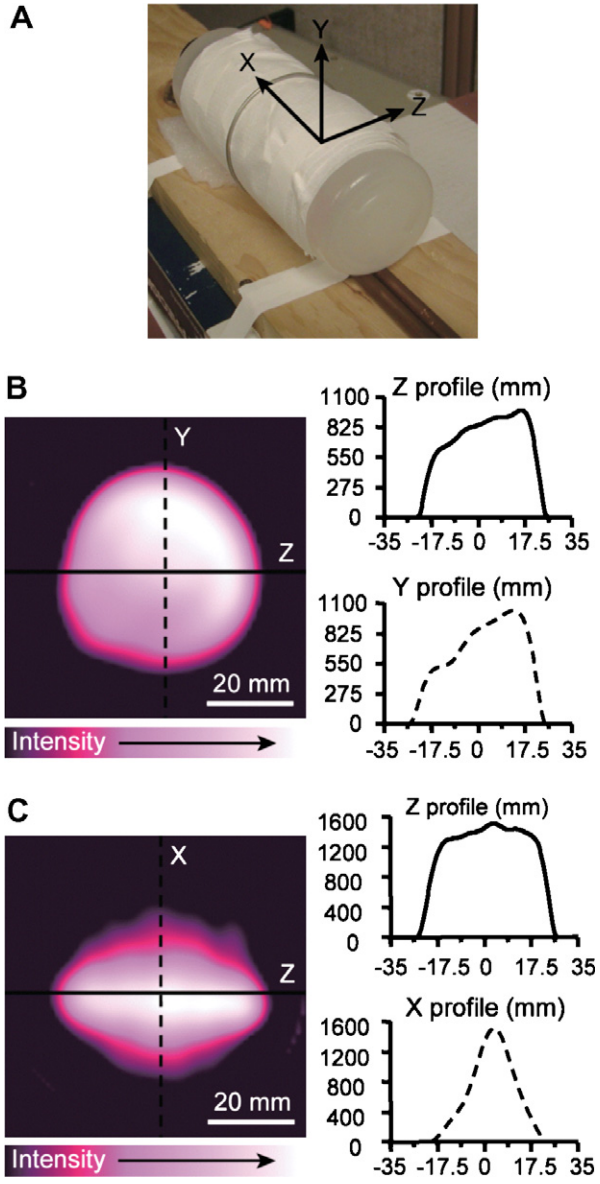

Fig. 6. EPR imaging of a phantom at 300 MHz. (A) The phantom was a cylindrical bottle of 49 mm in diameter and 140 mm long filled with 1 mM 3-CP in half water/half PBS solution. (B) 2D EPR image of the phantom in the ZY-plane. (C) 2D EPR image of the phantom in the ZX-plane. Imaging parameters are as follows: microwave power 2.0 W, magnetic field modulation 0.1 mT, field gradient 0.2 mT/cm, number of projections 64, FOV 70 mm, and acquisition time 11 min.

3-CP probes in the abdominal area. After 3-CP probes were injected into an anesthetized rat, weak EPR signals were detected in the first image (4 min, including liver and kidneys) in Fig. 7B. Their brightness then gradually increased (at 8, 12, and 16 min). At the same time, the image intensity in the bladder starts to build up (16 min). In the image in the ZX-plane in Fig. 7C (20 min), a prominent bright spot was visualized, and this should correspond to signals from 3-CP in the bladder. Since the 3-CP probe is distributed in different organs and tissues in the abdominal area of the rat, sharp images of individual organs are not obtained in these 2D acquisitions. The spatial resolution of these rat images was approximately 5 mm (Fig. 7B and C). If the 3D distribution of spin probes in a subject animal must be determined precisely, 3D EPR acquisitions must be performed and co-registration, as in EPR/NMR co-imaging, can be performed to provide an anatomical map of the location of free radicals in the body [8,27,36–38]. However, this is beyond the focus and scope of the present work.

4. Discussion

The resonator described here is highly efficient for generating an RF magnetic field, although the diameter of the loop is much larger than that of surface-coil resonators (SCR) that have been previously reported for operation at higher frequencies of 1.1–1.2 GHz. An electronically tunable SCR with a loop of 10 mm in diameter had an efficiency of 77 $\mu T/W^{1/2}$ [29,39]. While the loop of the resonator in this study was 5.5-fold larger than that of an SCR at 1.1 GHz, the resonator was almost half as efficient as the SCR. This finding suggests that sensitive EPR detec-

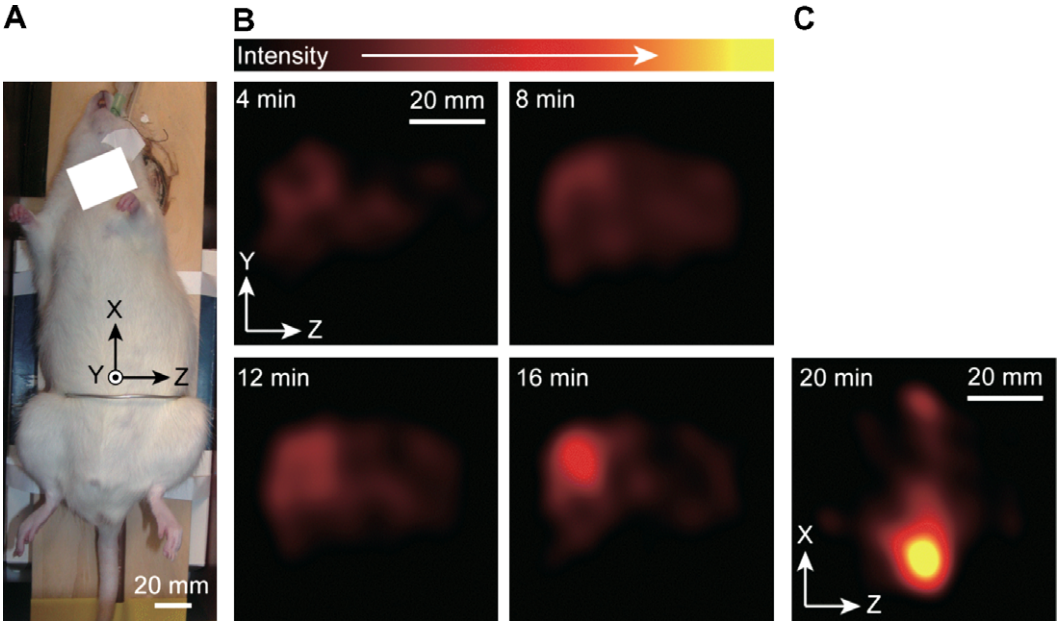

Fig. 7. (A) Photograph of a subject rat placed in the single-turn loop of the resonator. (B) In vivo rat imaging at 300 MHz. The rat was given 3 ml of 100 mM 3-CP PBS solution. A series of 2D EPR images in the ZY-plane were obtained with the following parameters: microwave power 1.6 W, magnetic field modulation 0.1 mT, field gradient 0.2 mT/cm, number of projections 16, FOV 70 mm, and acquisition time 4 min. (C) In vivo rat imaging at 300 MHz. The rat was given 3 ml of 100 mM 3-CP PBS solution. After 16 min of imaging, a 2D EPR image in the ZX-plane was obtained with the parameters noted in Fig. 7B.

tion for rats could be possible with the resonator. Magnetic flux density at the center of a circular current is inversely proportional to the radius of the current, if the intensity of flowing current is the same. This predicts that the efficiency for RF magnetic field generation will be 18% of that of the SCR at 1.1 GHz. In actuality, the loop resonator reported in this paper had a large portion of the stored magnetic energy in the resonator loop. The efficiency of the loop resonator was better than the predicted value, since the feeding circuit for the loop had less stored energy in the transmission line.

Since most of the RF magnetic energy is stored in the loop, the resonator is highly efficient for generating an RF magnetic field. In a tunable SCR, most of the RF magnetic energy is stored in the transmission lines [39]. In contrast, since the parallel transmission line was matched somewhat to the single-turn loop and the capacitive divider, both standing waves and traveling waves occur in the parallel transmission line. If the standing wave ratio in the transmission line is close to unity, the RF magnetic energy stored in the transmission line will be small. This should improve the efficiency for generating an RF magnetic field in the loop. The input impedance of the parallel transmission line could be matched to the balun by adjusting the trimmer capacitor C_M. A matching circuit using a capacitor in parallel connection was discussed by Rinard and his colleagues [40]. This allows us to use a capacitor with a relatively larger capacitance. In practice, this could be helpful for selecting an appropriate trimmer capacitor.

While the amplitude of the current of the loop is uniform at a low frequency or even DC, it is no longer uniform at a higher frequency. When the circumference of the loop is not very short in comparison to the wavelength of the electromagnetic waves at a given frequency, the current intensity and the potential on the loop are distributed. The weaker current in the loop near the capacitor C_1 results in a relatively weak RF magnetic field. This is consistent with the results of the profile of an EPR image in Fig. 6B.

Slice-selective 2D EPR imaging could be obtained with the resonator. The resonator has a slice-selective sensitive region within and near the plane of the loop, and its effective width (full width at half maximum) was approximately 17 mm, as shown in Fig. 6C. Of course, a "slice" with the resonator is not the same as a slice in MRI. For the resonator, a "slice" is a thick slab (17 mm) with a non-uniform thickness, as shown in Fig. 6C. The localized width provided by this resonator is ideally suited for imaging of regions of special interest, such as the heart and brain. A much higher slice resolution within these localized regions of interest is provided by 3D spatial EPR imaging of these regions. Within these acquisitions, much finer slice resolutions can be readily obtained [3]. MRI usually shows slice images, since nuclear spins can be selectively excited in a slice. In contrast, since a protocol of a constant field gradient and field scanning cannot select a slice in standard 2D CW-EPR imaging, a 2D-EPR image shows the spatial distribution of unpaired electrons that is given from signals integrated in the depth direction. Therefore, a localized RF magnetic field, i.e., excitation of unpaired electrons in a quasi-slice region, is useful for visualizing a specific location, even if the slice selection is not uniform and thin as in MRI.

We successfully demonstrated EPR imaging of the lower abdomen in the rat using the loop resonator. The resonator could provide sufficient space for a rat with a body weight of 350 g. As shown in Fig. 7C, strong signals were detected for up to 30 min after bolus injection of the 3-CP nitroxide probe. Based on the observed EPR images, the distribution of the probe could be determined and its clearance from the body was followed. The spatial distribution of free radicals in subject animals is of critical importance for the investigation of organ-specific disease mechanisms in a broad range of biomedical applications. Moreover, the time-dependent distribution of spin probes must be determined to better understand drug delivery and redox status in specific organs. The resonator described here facilitates efforts to obtain this information and provide images of free radical probes within living rats. There have been few previous reports on EPR imaging in rats, which was difficult due to a lack of highly sensitive RF resonators that could provide sufficient space for a rat body. As we demonstrated here, the resonator described makes it possible to measure and image free radicals within selected regions of the rat body.

The sensitive region of the loop resonator shown in Fig. 6B and C was within the volume that had good homogeneity of the magnetic modulation field and linearity of field gradients. When a relatively large subject is measured, we have to be careful regarding the homogeneity of the magnetic modulation field and the linearity of field gradients over the subject being measured. The skin depth of a magnetic field modulated at 100 kHz can be estimated to be 1.6 m in 0.1 M sodium chloride solution (dielectric constant of 78 and conductivity of 1.0 S/m at 100 kHz) [41]. While a solution of half water/half PBS or the in vivo rat is not exactly the same as 0.1 M sodium chloride solution, it is clear that these samples do not affect magnetic field modulation because of the estimated skin depth.

The resonator has the following benefits: (i) highly efficient at generating an RF magnetic field, (ii) simple structure that is easy to implement, (iii) simple matching circuit, (iv) high-power capability of more than 1 W, (v) slice-selective sensitivity distribution in the loop, and (vi) no RF shielding required. Technical issues for future work are: (i) remote control of impedance matching and the resonance frequency of the resonator, (ii) optimization of the efficiency for generating the RF magnetic field, and (iii) mechanical implementation of the loop resonator for intensive use in animal experiments. A systematic method for the further design of the loop resonator may be helpful for use at other frequencies and in specific biomedical applications.

The sensitive region of the loop resonator is limited as shown in Figs. 4 and 6. If whole-body imaging on rats is required, multiple measurements could be carried out so that the position of the loop moves along the orientation of the body of the rat from head to tail. However, it would take a longer time, which is a function of the number of images and the acquisition time for a single image. In perspective, multi-channel acquisition techniques analogous to those that have been developed for proton MRI could be helpful for whole-body EPR imaging of the rat. However, to date, multi-channel acquisition has not yet been achieved in CW-EPR imaging. This is because the detection schemes are different between CW-EPR imaging and multi-channel detection in MRI, which is based on pulsed protocols. If a multi-channel acquisition technique is developed for whole-body EPR imaging, it would have tremendous impact on free-radical-related studies in small animals. However, this can not be achieved by simple extension of the approach used in pulsed MRI. In CW-EPR with a reflection bridge, the power is continuously applied to the coil, which is close to critically coupled. Thus, it is quite difficult to achieve the requisite level of decoupling required for parallel array detection. This goal of parallel array detection is highly desirable, but to achieve it may require switching to a pulsed EPR approach and this comes at the cost of diminished sensitivity and problems with system dead time that limit detection to EPR probes with very long relaxation times. Common spin probes such as nitroxides or nitric oxide (NO) spin trap complexes can not be detected with pulsed techniques at 300 MHz because of the system dead times. Thus, there is a need for optimized CW-EPR instrumentation and resonators at this frequency, as described in this article.

5. Conclusions

For a resonator consisting of a single-turn loop of 55 mm in diameter, an RF magnetic field of 38 $\mu T/W^{1/2}$ was generated of high efficiency. This resonator provides sufficient space for the placement and imaging of a rat. Slice-selective EPR imaging of a living rat was demonstrated with the loop resonator. After the infusion of a nitroxide probe, EPR images in the abdominal region were obtained sequentially, and this enabled visualization of the time course of radical clearance within the body of the living rat. This resonator enables the specific EPR detection and visualization of paramagnetic molecules in any desired axial region of the rat. Thus, it should facilitate the application of the powerful techniques of EPR spectroscopy and imaging to in vivo applications for studying normal physiology and disease in rat models.

Acknowledgments

The authors thank Eric Kesselring for his technical assistance with the 300 MHz CW-EPR imager. The authors are also grateful to Dr. Yangsong Wu for his assistance with animal preparation. This work was supported in part by NIH grants (EB00254, EB00890, and EB004900 to J.L.Z.), the Japan Society for the Promotion of Science (18360194 to H.H.), and the Industrial Technology Research Grant Program in 2004 from the New Energy and Industrial Technology Development Organization (NEDO) of Japan (04A06006 to H.H.).

References

[1] P. Kuppusamy, M. Chzhan, K. Vij, M. Shteynbuk, D.J. Lefer, E. Giannella, J.L. Zweier, Three-dimensional spectral-spatial EPR imaging of free radicals in the heart: a technique for imaging tissue metabolism and oxygenation, Proc. Natl. Acad. Sci. USA 91 (1994) 3388–3392.

[2] T. Yoshimura, H. Yokoyama, S. Fujii, F. Takayama, K. Oikawa, H. Kamada, In vivo EPR detection and imaging of endogenous nitric oxide in lipopolysaccharide-treated mice, Nat. Biotechnol. 14 (1996) 992–994.

[3] G. He, R.A. Shankar, M. Chzhan, A. Samouilov, P. Kuppusamy, J.L. Zweier, Noninvasive measurement of anatomic structure and intraluminal oxygenation in the gastrointestinal tract of living mice with spatial and spectral EPR imaging, Proc. Natl. Acad. Sci. USA 96 (1999) 4586–4591.

[4] B.B. Williams, H.J. Halpern, In vivo EPR imaging, in: S.S. Eaton, G.R. Eaton, L.J. Berliner (Eds.), Biomedical EPR Part A: Free Radicals, Metals, Medicine, and Physiology, Biological Magnetic Resonance, vol. 23, Kluwer Academic, New York, 2005, pp. 283–317.

[5] J.A. Brivati, A.D. Stevens, M.C.R. Symons, A radiofrequency ESR spectrometer for in vivo imaging, J. Magn. Reson. 92 (1991) 480–489.

[6] K. Oikawa, H. Togashi, R. Kudo, N. Kainuma, H. Ohya, H. Kamada, Development of 300 MHz ESR-CT system, in: Proceedings of Joint Symposium on Bio-Sensing and Bio-Imaging 2001, Yamagata, Japan, 2001, pp. 193–195.

[7] K.H. Ahn, V.S. Subramanian, C. Mailer, X. Pan, H.J. Halpern, Scaling of EPR spectra-spatial images: images of samples greater than 5 cm in linear dimension, in: Abstracts of 47th Rocky Mountain Conference on Analytical Chemistry, Denver, Colorado, USA, 2005, p. 45.

[8] M. Alecci, I. Seimenis, S.J. McCallum, D.J. Lurie, M.A. Foster, Nitroxide free radical clearance in the live rat monitored by radiofrequency CW-EPR and PEDRI, Phys. Med. Biol. 43 (1998) 1899–1905.

[9] X. Zhang, K. Ugurbil, W. Chen, Microstrip RF surface coil design for extremely high-field MRI and spectroscopy, Magn. Reson. Med. 46 (2001) 443–450.

[10] J. Wang, Q.X. Yang, X. Zhang, C.M. Collins, M.B. Smith, X.-H. Zhu, G. Adriany, K. Ugurbil, W. Chen, Polarization of the RF field in a human head at high field: a study with a quadrature surface coil at 7.0 T, Magn. Reson. Med. 48 (2002) 362–369.

[11] F. Mirrashed, J.C. Sharp, I. Cheung, B. Tomanek, High-resolution imaging at 3 T and 7 T with multiring local volume coils, Magn. Reson. Mater. Phys. 16 (2004) 167–173.

[12] J. Pheuffer, H. Merkle, M. Beyerlein, T. Steudel, N.K. Logothetis, Anatomical and functional MR imaging in the macaque monkey using a vertical large-bore 7 Tesla setup, Magn. Reson. Imag. 22 (2004) 1343–1359.

[13] L.L. Wald, G.C. Wiggins, A. Potthast, C.J. Wiggins, C. Triantafyllou, Design considerations and coil comparisons for 7 T and 9 T brain imaging, Appl. Magn. Reson. 29 (2005) 19–37.

[14] G.C. Wiggins, A. Potthast, C. Triantafyllou, C.J. Wiggins, L.L. Wald, Eight-channel phased array coil and detunable TEM volume coil for 7 T brain imaging, Magn. Reson. Med. 54 (2005) 235–240.

[15] T.S. Ibrahim, A. Kangarlu, D.W. Chakeress, Design and performance issues of RF coils utilized in ultra high field MRI: experimental and numerical evaluations, IEEE Trans. Biomed. Eng. 52 (2005) 1278–1284.

[16] T. Vaughan, L. DelaBarre, C. Snyder, J. Tian, C. Akgun, D. Shrivastava, W. Liu, C. Olson, G. Adriany, J. Strupp, P. Andersen, A. Gopinath, P.-F. van de Moortele, M. Garwood, K. Ugurbil, 9.4 T human MRI: preliminary results, Magn. Reson. Med. 56 (2006) 1274–1282.

[17] C. Wang, G.X. Shen, B_1 field, SAR, and SNR comparisons for birdcage, TEM, and microstrip coils at 7 T, J. Magn. Reson. Imag. 24 (2006) 439–443.

[18] I. Nicholson, M.A. Foster, F.J.L. Robb, J.M.S. Hutchison, D.J. Lurie, In vivo imaging of nitroxide-free-radical clearance in the rat, using radiofrequency longitudinally detected ESR imaging, J. Magn. Reson. Ser. B 113 (1996) 256–261.

[19] M.A. Foster, I.A. Grigor'ev, D.J. Lurie, V.V. Khramtsov, S. McCallum, P. Panagiotelis, J.M.S. Hutchison, A. Koptioug, In vivo detection of a pH-sensitive nitroxide in the rat stomach by low-field ESR-based techniques, Magn. Reson. Med. 49 (2003) 558–567.

[20] M.A. Foster, I. Seimenis, D.J. Lurie, The application of PEDRI to the study of free radicals in vivo, Phys. Med. Biol. 43 (1998) 1893–1897.

[21] I. Seimenis, M.A. Foster, D.J. Lurie, J.M.S. Hutchison, P.H. Whiting, S. Payne, Chemically induced analgesic nephropathy in the rat monitored by proton–electron on double-resonance imaging (PEDRI), Magn. Reson. Med. 40 (1998) 280–286.

[22] Y. Deng, G. He, S. Petryakov, P. Kuppusamy, J.L. Zweier, Fast EPR imaging at 300-MHz using spinning magnetic field gradients, J. Magn. Reson. 168 (2004) 220–227.

[23] M. Afeworki, G.M. van Dam, N. Devasahayam, R. Murugesan, J. Cook, D. Coffin, J.H.A.- Larsen, J.B. Mitchell, S. Subramanian, M.C. Krishna, Three-dimensional whole body imaging of spin probes in mice by time-domain radiofrequency electron paramagnetic resonance, Magn. Reson. Med. 43 (2000) 375–382.

[24] S. Subramanian, N. Devasahayam, R. Murgesan, K. Yamada, J. Cook, A. Taube, J.B. Mitchell, J.A.B. Lohman, M.C. Krishna, Single-point (constant-time) imaging in radiofrequency Fourier transform electron paramagnetic resonance, Magn. Reson. Med. 48 (2002) 370–379.

[25] C. Mailer, S.V. Sundramoorthy, C.A. Pelizzari, H.J. Halpern, Spin echo spectroscopic electron paramagnetic resonance imaging, Magn. Reson. Med. 55 (2006) 904–912.

[26] J. Murphy-Boesch, A.P. Koretsky, An in vivo NMR probe circuit for improved sensitivity, J. Magn. Reson. 54 (1983) 526–532.

[27] Y. Kawada, H. Hirata, H. Fujii, Use of multi-coil parallel-gap resonators for co-registration EPR/NMR imaging, J. Magn. Reson. 184 (2007) 29–38.

[28] H.J. Halpern, D.P. Spencer, J. van Polen, M.K. Bowman, A.C. Nelson, E.M. Dowey, B.A. Teicher, Imaging radio frequency electron-spin-resonance spectrometer with high resolution and sensitivity for in vivo measurements, Rev. Sci. Instrum. 60 (1989) 1040–1050.

[29] H. Hirata, T. Walczak, H.M. Swarts, Electronically tunable surface-coil-type resonator for L-band EPR spectroscopy, J. Magn. Reson. 142 (2000) 159–167.

[30] H. Yokoyama, T. Sato, T. Ogata, H. Ohya, H. Kamada, Automatic coupling control of a loop-gap resonator by a variable capacitor attached coupling coil for EPR measurements at 650 MHz, J. Magn. Reson. 149 (2001) 29–35.

[31] G. He, S. Petryakov, A. Samoulilov, M. Chzhan, P. Kuppusamy, J.L. Zweier, Development of a resonator with automatic tuning and coupling capability to minimize sample motion noise for in vivo EPR spectroscopy, J. Magn. Reson. 149 (2001) 218–227.

[32] J.J.H. Wang, Generalized Moment Methods in Electromagnetics, John Wiley & Sons, New York, 1991, pp. 508–538.

[33] H. Lei, O. Grinberg, C.I. Nwaigwe, H.G. Hou, H. Williams, H.M. Swartz, J.F. Dunn, The effects of ketamine–xylazine anesthesia on cerebral blood flow and oxygenation observed using nuclear magnetic resonance perfusion imaging and electron paramagnetic resonance oximetry, Brain. Res. 913 (2001) 174–179.

[34] J.H. Freed, D.S. Leniart, J.S. Hyde, Theory of saturation and double resonance effects in ESR Spectra. III. rf coherence and line shapes, J. Chem. Phys. 47 (1967) 2762–2773.

[35] G. He, S.P. Evalappan, H. Hirata, Y. Deng, S. Petryakov, P. Kuppusamy, J.L. Zweier, Mapping of the B_1 field distribution of a surface coil resonator using EPR imaging, Magn. Reson. Med. 48 (2002) 1057–1062.

[36] G. He, Y. Deng, H. Li, P. Kuppusamy, J.L. Zweier, EPR/NMR co-imaging for anatomic registration of free-radical images, Magn. Reson. Med. 47 (2002) 571–578.
[37] S. Matsumoto, M. Nagai, K. Yamada, F. Hyodo, K. Yasukawa, M. Muraoka, H. Hirata, M. Ono, H. Utsumi, A composite resonator assembly suitable for EPR/NMR coregistration imaging, Concepts Magn. Reson. Part B: Magn. Reson. Eng. 25B (2005) 1–11.
[38] F. Hyodo, K. Yasukawa, K. Yamada, H. Utsumi, Spatially resolved time-course studies of free radical reactions with an EPRI/MRI fusion technique, Magn. Reson. Med. 56 (2006) 938–943.
[39] H. Hirata, T. Walczak, H.M. Swarts, Characteristics of an electronically tunable surface-coil-type resonator for L-band electron paramagnetic resonance spectroscopy, Rev. Sci. Instrum. 72 (2001) 2839–2841.
[40] G.A. Rinard, R.W. Quine, S.S. Eaton, G.R. Eaton, Microwave coupling structures for spectroscopy, J. Magn. Reson. Ser. A 105 (1993) 137–144.
[41] Laboratory for Insulation Research MIT, Tables of dielectric materials, in: A. von Hippel (Ed.), Dielectric Materials and Applications, John Wiley & Sons, New York, 1954, pp. 291–425.